https://doi.org/10.1016/j.electacta.2019.04.076

Phase field study of mechanico-electrochemical corrosion

Chen Lin[a], Haihui Ruan[a, *], San-Qiang Shi[a, b, *]

[a] Department of Mechanical Engineering, The Hong Kong Polytechnic University, Hong Kong, China

[b] The Hong Kong Polytechnic University Shenzhen Research Institute, Shenzhen, China

Abstract

A phase field (PF) model was proposed to investigate corrosion in a stressed metal. The Allen–Cahn equation, associated with the Nernst–Planck, Poisson's, and mechanical equilibrium equations, was established to govern phase transformation, ion diffusion, electric potential field, and mechanical deformation. A corrosion rate equation was incorporated to describe the migration of the metal phase boundary, which is expressed based on a detailed balance in the electrochemical reaction and conforms to a generalized Butler–Volmer equation. The numerical results revealed that the stress concentration at the tip of a corrosion pit promotes a higher corrosion rate; this results in a sharpening of the tip that can cause accelerated failure of the metal structure. To consider a more complicated scenario, a metal matrix composite (MMC) reinforced with inert fibers/particles was investigated. If a fixed displacement boundary condition is applied, the corrosion resistance of the MMC would benefit from the decrease in the reinforcement stiffness; meanwhile, when the MMC is under a constant load, a stiffer reinforcement would result in an increase in the corrosion resistance.

---

[*] Corresponding author Tel.: + 852 2766 6648, Fax: +852 2365 4703, E-mail address: haihui.ruan@polyu.edu.hk

Corresponding author Tel.: + 852 2766 7821, Fax: +852 2766 7821, E-mail address: mmsqshi@polyu.edu.hk

Keyword: *Pitting corrosion; Electrochemical mechanism; Mechanical deformation; Phase field model.*

Nomenclature

$\mathbf{c}$	Concentration vector
$\boldsymbol{\varphi}$	Electric potential vector
$\mathbf{d}$	Displacement vector
$\boldsymbol{\varepsilon}$	Total strain
$\mathbf{D}^{\mathrm{e}}$	Elastic stiffness matrix
$\boldsymbol{\sigma}$	Stress tensor
K_{I}	Stress intensity factor for type I crack
F	Total Gibbs free energy
f	Free energy density
μ	Chemical potential
ΔE	Electric potential difference
ΔE_{eq}	Equilibrium electric potential difference
η	Overpotential
ϕ	Phase order parameter
λ	Scale factor of the interfacial energy density
S	Interfacial energy density
ζ	Interfacial thickness
ρ	Asymmetry factor
r	Reaction rate
L_S	Coefficient of the contribution of interfacial energy
L_κ	Coefficient of the contribution of reaction kinetics
D	Diffusion coefficient
ς	Charge–density change per unit time
div	Divergence operator
∇	Gradient operator
∂	Partial differential symbol
δ	Variational symbol

1. Introduction

In general, in a complex service environment, corrosion of metallic materials occurs; this results in the degradation of the integrity and durability of mechanical components. Therefore, a few metallic materials are alloyed with active-passive metals such as aluminum or chromium to form a passive film on the surface; this resists further corrosion. However, the partial breakdown of the passive film may result in excessively localized corrosion pits [1, 2]. The local pitting may cause the initiation and extension of microcracks under mechanical loading, which accelerates failure. An understanding of the mechanism of pitting corrosion under mechanical loading would aid in predicting the failure of metallic structures and in improving the design of structure materials.

Numerous theoretical and numerical approaches have been proposed for studying pitting corrosion. In the 1970s, theoretical studies were conducted by Newman *et al.* [3, 4], Yahalom *et al.* [5], and Mccafferty *et al.* [6] for one-dimensional (1D) corrosion; herein, the Laplace equation was employed to solve electric potential distribution, and Ohm's law was adopted to relate current density to potential gradient. To extend these theoretical studies to more general scenarios, numerical models based on the finite difference method (FDM) were proposed [7-13]; these involved the Nernst–Planck equation for describing elemental diffusion impelled by gradient of concentration and electric potential. However, the morphological evolution of a corroded pit was challenging to address using the FDM. Assuming sharp interfaces, the moving boundary problem was solved based on the finite volume method (FVM) [14], finite element method (FEM) [15], extended finite element method (XFEM) [17], and nonlocal peridynamic (PD) modeling [18]. However, the interfacial tracking requires *ad hoc* assumptions with regard to the interfacial geometry; this significantly affects the accuracy and convergence of numerical simulations.

The phase field (PF) method, which developed rapidly in the last two decades, has been used for analyzing phase evolution in materials. The PF method employs a diffusive interface to address complex morphology variations without explicitly tracking the interface positions. By coupling with the effects of various physical, chemical, and mechanical fields, the PF method has been extended and utilized to predict numerous material processes. A few applications of the PF method for the corrosion process have also been proposed [20-24]. Based on the Kim–Kim–Suzuki (KKS) model [19], Mai *et al.* [20, 21] proposed a PF model to describe pitting and galvanic corrosion. In their model, interface migration was governed by the Allen–Cahn equation with a current–density-dependent interface kinetics parameter. The ion transport was regulated by the Cahn–Hilliard equation. However, they did not consider ion production (or consumption) during the electrochemical reaction, or the effect of electric potential gradients on ion diffusion. In Ansari *et al.'s* PF model for pitting corrosion [22], the interface kinetics parameter was related to the exchange current density based on the Butler–Volmer relationship; moreover, the overpotential was dependent on the metal ion concentration and on the transport and reactions of the ionic species in the electrolyte. Stress corrosion cracking (SCC) was also studied. Mai *et al.* [23] assumed a linear relation between the equivalent stress and the interface kinetics parameter; moreover, they employed the von Mises yield criterion to describe ductile cracking. Nguyen *et al.* [24] considered the contribution of chemical potential and elastic energy densities in Gibbs free energy. Their formula for interface migration involved the ion diffusion rate and the elastic energy release rate, which describes the SCC of a brittle material. In the SCC models of Mai *et al.* [23] and Nguyen *et al.* [24], the influence of the electrostatic field was not considered. In addition, in the above PF models, the chemical (or electrochemical) reaction rate was assumed to be stress-independent. However, numerous experimental studies [25, 26] have demonstrated that chemical (or electrochemical) reaction kinetics could be affected by mechanical stresses. For example, Zhu *et al.* [25] experimentally observed that a metallic sample under both tensile and compressive stress states could be more straightforwardly corroded than one in a stress-free state.

In the present study, we proposed a PF model to investigate mechanico-electrochemical corrosion. The electrochemical reaction rate was expressed as a function of the electrochemical potentials of the reactants and products, based on a detailed balance of the reactions; moreover, it conforms to a generalized Butler–Volmer relationship. The Gibbs free energy was established, in which the contributions of the chemical potential, interface, electrostatic field, and mechanical deformation are considered. Thus, the electrochemical potentials, which are the variational derivatives of free energy density with respect to the elemental concentrations, were derived. Considering that the consumption of the metallic phase is a consequence of corrosion, the rate of corrosion and rate of phase transformation are equalized. Consequently, a generalized Allen–Cahn type equation that captures the corrosion kinetics and the effects of variations in elemental concentration, electric potential, and elastic energy was established to govern the evolution of the metallic phase. Coupled with the generalized Nernst–Planck equation, Poisson’s equation, and the mechanical equilibrium equation, the proposed PF model was applied to study the mechanico-electrochemical pitting corrosion in pure metal and in fiber/particle-reinforced metal matrix composite (MMC).

2. Methodology

Figure 1 shows the local breakdown in a passive film that results in the growth of a corrosion pit in salt water. With the applied anodic potential (+), φ, the metal (M) would corrode and release metal cations (M^{n+}) into the electrolyte:

$$\mathrm{M} \rightarrow \mathrm{M}^{\mathrm{n}+} + ne^{-}, \tag{1}$$

where the electrons (e^-) flow in the metal to the cathode surface (-) and induce cathodic reactions. In the present model, we assumed that the cathode reactions are rapid enough so that they do not affect the reactions at the anode. Thus, only the anode reaction, expressed in Eq. (1), was considered. If the cathode becomes the rate-limiting electrode, the effect of the cathodic reaction must be involved; it can also be incorporated in the framework of the present model (see Appendix C). We also considered the scenario wherein the metallic component is under mechanical loading.

Fig. 1

2.1. Gibbs free energy for the mechanico-electrochemical system

Denoting the set of elemental concentrations as **c**, displacement field as **d**, and electrostatic field as **φ**, the Gibbs free energy of the system can be expressed as

$$\mathrm{F} = \int_{\Omega} f d\omega, \tag{2a}$$

$$\text{and} \quad f = f_{\mathrm{chem}}(\mathbf{c}) + f_{\mathrm{grad}}(\mathbf{c}) + f_{\mathrm{mech}}(\mathbf{c},\mathbf{d}) + f_{\mathrm{elec}}(\mathbf{c},\boldsymbol{\varphi}), \tag{2b}$$

where F is the total Gibbs free energy of a closed system, Ω; f is the free energy density; and $d\omega$ is the volume infinitesimal element for the system Ω. As expressed in Eq. (2b), the free energy density can be divided into the chemical potential energy density, f_{chem}, gradient energy density, f_{grad}, mechanical energy density, f_{mech}, and electric potential energy density, f_{elec}. Herein, the set of elemental concentrations can be expressed as $\mathbf{c} = (c^{\mathrm{M}}, c^{\mathrm{M}^{n+}}, c^{\mathrm{e}^-})$; here, the superscripts $^{\mathrm{M}}$, $^{\mathrm{M}^{n+}}$, and $^{\mathrm{e}^-}$ pertain to the metal (M), metal cation (M^{n+}), and electron (e^-), respectively. The concentrations can be further expressed in the dimensionless form, $\bar{c} = c / c_{\mathrm{ref}}$; here, the subscript "ref" indicates the reference concentration. Omitting the mutual interaction between different species and the effect of electrons (assuming that electrons flow to the cathode in zero time), the chemical potential energy density can be expressed as

$$f_{\mathrm{chem}}\left(\mathbf{c}\right)=Wg\left(\bar{c}^{\mathrm{M}}\right)+c^{\mathrm{M^{n+}}}RT\ln\left(\bar{c}^{\mathrm{M^{n+}}}\right)+c^{\mathrm{M^{n+}}}\left(\mu_0^{\mathrm{M^{n+}}}-RT\right), \tag{3}$$

where R is the ideal gas constant, T is the thermodynamic temperature, and μ_0 is the standard chemical potential. The first term on the right-hand side is a double-well function, $g\left(\bar{c}^{\mathrm{M}}\right)=\left(\bar{c}^{\mathrm{M}}\right)^2\left(1-\bar{c}^{\mathrm{M}}\right)^2$, describing the energy barrier between the solid (*i.e.*, the metal (M)) and liquid (*i.e.*, the electrolyte) phases; it has minima at $\bar{c}^{\mathrm{M}}=1$ (solid phase) and $\bar{c}^{\mathrm{M}}=0$ (liquid phase) and is symmetric about $\bar{c}^{\mathrm{M}}=0.5$. W is the height of the energy barrier for the phase transformation (corrosion); it is related to the interfacial energy (per unit area), S, and the interface thickness, ζ, as $W=18S/\zeta$ [27].

With a diffuse interface between the solid and liquid phases, the gradient energy density, f_{grad} ($\mathbf{c}$), can be expressed as

$$f_{\mathrm{grad}}\left(\mathbf{c}\right)=\frac{\lambda}{2}\left|\nabla\bar{c}^{\mathrm{M}}\right|^2, \tag{4}$$

where ∇ is the gradient operator and λ is the scale factor of the interfacial energy density. It is established that if the interface is isotropic with energy density (per unit area) S and thickness ζ, $\lambda=S\zeta$ [27].

The mechanical energy density, f_{mech}, in Eq. (2b) is defined as

$$f_{\mathrm{mech}}\left(\mathbf{c},\mathbf{d}\right)=p\left(\bar{c}^{\mathrm{M}}\right)f_{\mathrm{mech}}^{\mathrm{M}}, \tag{5}$$

where $p\left(x\right)$ is the interpolation function. Equation (5) satisfies the conditions that the elastic energy density is continuous at any value of displacement, $\boldsymbol{d}$, and that f_{mech} (x, $\boldsymbol{d}$) has local minima with respect to x at $x=0$ and $x=1$. Following Wang *et al.* [28], an appropriate formula for $p(x)$ can be specified: $p\left(x\right)=x^3\left(10-15x+6x^2\right)$. $f_{\mathrm{mech}}^{\mathrm{M}}$ is the mechanical energy density of the solid phase; it is expressed as

$$f_{\text{mech}}^{\text{M}} = \frac{1}{2}\left(\left(\boldsymbol{\varepsilon}^{\text{e}}\right)^{T} \cdot \left(\mathbf{D}^{\text{e}}\boldsymbol{\varepsilon}^{\text{e}}\right)\right), \tag{6}$$

where $\mathbf{D}^{\text{e}}$ is the stiffness matrix of the solid phase and $\boldsymbol{\varepsilon}^{\text{e}}$ is the elastic strain tensor, which is derived from the geometric relation under an assumption of marginal deformation:

$$\boldsymbol{\varepsilon}^{\text{e}} = \left\{\varepsilon_{ij}^{\text{e}}\right\} = \left\{\frac{1}{2}\left(\frac{\partial d_i}{\partial x_j} + \frac{\partial d_j}{\partial x_i}\right)\right\} \ \left(i = 1, 2, 3;\ j = 1,2,3\right). \tag{7}$$

In Eq. (7), d_i and d_j are the components of the displacement field, $\mathbf{d}$.

The electric potential energy density, f_{elec}, in Eq. (2), is expressed as [29]

$$f_{\text{elec}}\left(\mathbf{c}, \boldsymbol{\varphi}\right) = F\left(nc^{\text{M}^{n+}}\varphi - c^{\text{e}^-}\varphi_{\text{S}}\right), \tag{8}$$

where F is the Faraday constant and φ and φ_{S} are the applied electrostatic potential and the electrostatic potential in the metal, respectively. The distribution of electrostatic potential in the metal is uniform, *i.e.*, φ_{S} is a constant.

2.2. Mechanico-electrochemical corrosion kinetics

Corrosion is a kinetic process involving both forward and backward reactions. If the forward reaction is more favorable, the metal becomes corroded. To describe the kinetics, the forward and backward reaction rates that satisfy a detailed balance of the electrochemical system [30] are expressed as

$$r_{1\to 2} = k_0 e^{-\left(\mu_{\text{TS}}^{\text{ex}} - \mu_1\right)/RT}, \tag{9a}$$

$$r_{2\to 1} = k_0 e^{-\left(\mu_{\text{TS}}^{\text{ex}} - \mu_2\right)/RT} \tag{9b}$$

and the net reaction rate is

$$r_{\text{net}} = r_{1\to 2} - r_{2\to 1} = k_0\left(e^{-\left(\mu_{\text{TS}}^{\text{ex}} - \mu_1\right)/RT} - e^{-\left(\mu_{\text{TS}}^{\text{ex}} - \mu_2\right)/RT}\right), \tag{9c}$$

where $r_{1\to 2}$, $r_{2\to 1}$, and r_{net} represent the forward, backward, and net reaction rates, respectively; μ_1 and μ_2 are the electrochemical potential at the initial (metal) and final (metal ion) states, respectively; $\mu_{\mathrm{TS}}^{\mathrm{ex}}$ is the excess chemical potential at the transition state; and k_0 is the rate constant. Based on Eq. (1), μ_1 and μ_2 are the variational derivatives of the total free energy, F, with respect to the corresponding concentration [31] and are expressed as

$$\mu_1 = \frac{\delta \mathrm{F}}{\delta c^{\mathrm{M}}} = \frac{1}{c_{\mathrm{ref}}^{\mathrm{M}}}\left(W \frac{\partial g\left(\bar{c}^{\mathrm{M}}\right)}{\partial \bar{c}^{\mathrm{M}}} - \lambda \nabla^2 \bar{c}^{\mathrm{M}} \right) + \frac{\partial p\left(\bar{c}^{\mathrm{M}}\right)}{\partial \bar{c}^{\mathrm{M}}} \frac{f_{\mathrm{mech}}^{\mathrm{M}}}{c_{\mathrm{ref}}^{\mathrm{M}}} \tag{10a}$$

and $$\mu_2 = \frac{\delta \mathrm{F}}{\delta c^{\mathrm{M}^{\mathrm{n+}}}} + n \frac{\delta \mathrm{F}}{\delta c^{\mathrm{e}^-}} = RT \ln \bar{c}^{\mathrm{M}^{\mathrm{n+}}} + \mu_0^{\mathrm{M}^{\mathrm{n+}}} - nF\Delta E \,, \tag{10b}$$

where δ is the variational symbol and $\Delta E = \varphi_{\mathrm{S}} - \varphi$ is the electric potential difference at the interface between the metallic material and electrolyte.

Following Bazant *et al.* [30], the electrochemical potential can be further expressed as

$$\mu_{1\ (\mathrm{or}\ 2)} = \mu_{1\ (\mathrm{or}\ 2)}^{\mathrm{diff}} + \mu_{1\ (\mathrm{or}\ 2)}^{\mathrm{ex}} \,, \tag{11}$$

where μ^{diff} is the chemical potential driven by the concentration gradient and μ^{ex} is the excess chemical potential that originates from mechanical deformation, applied electrostatic field, etc., *i.e.*,

$$\mu_{1\ (\mathrm{or}\ 2)}^{\mathrm{ex}} = \mu_{1\ (\mathrm{or}\ 2)}^{\Gamma} + \mu_{1\ (\mathrm{or}\ 2)}^{\Theta} + \mu_{1\ (\mathrm{or}\ 2)}^{\mathrm{elec}} \,. \tag{12}$$

In Eq. (12), μ^{Γ} represents the non-ideal component of the electrochemical potential; in the present model, it is contributed by mechanical deformation. μ^{Θ} and μ^{elec} are the reference chemical potential and electric potential, respectively. It is apparent that without corrosion, $\mu_1^{\Gamma} \neq 0$, $\mu_1^{\Theta} = \mu_1^{\mathrm{elec}} = 0$, and only the mechanical deformation contributes to the excess chemical potential. After the metal is corroded, the cations are dissolved in the electrolyte, which cannot withstand mechanical loading. Therefore, $\mu_2^{\Gamma} = 0$; moreover, the excess chemical potential is owing to the additional cations and electric field, expressed as $\mu_2^{\Theta} = \mu_0^{\mathrm{M}^{n+}}$ and $\mu_2^{\mathrm{elec}} = -nF\Delta E$, respectively. Thus, $\mu_{1\,(\mathrm{or}\,2)}^{\mathrm{diff}}$ and $\mu_{1\,(\mathrm{or}\,2)}^{\mathrm{ex}}$ are expressed as

$$\mu_1^{\mathrm{diff}} = \frac{1}{c_{\mathrm{ref}}^{\mathrm{M}}}\left(W \frac{\partial g\left(\bar{c}^{\mathrm{M}}\right)}{\partial \bar{c}^{\mathrm{M}}} - \lambda \nabla^2 \bar{c}^{\mathrm{M}} \right), \tag{13a}$$

$$\mu_1^{\mathrm{ex}} = \frac{\partial p\left(\bar{c}^{\mathrm{M}}\right)}{\partial \bar{c}^{\mathrm{M}}} \frac{f_{\mathrm{mech}}^{\mathrm{M}}}{c_{\mathrm{ref}}^{\mathrm{M}}}, \tag{13b}$$

$$\mu_2^{\mathrm{diff}} = RT \ln \bar{c}^{\mathrm{M}^{n+}}, \tag{13c}$$

respectively, and

$$\mu_2^{\mathrm{ex}} = \mu_0^{\mathrm{M}^{n+}} - nF\Delta E\,. \tag{13d}$$

Following Bazant *et al.* [30], the excess chemical potential in the transition state, $\mu_{\mathrm{TS}}^{\mathrm{ex}}$, is defined as

$$\mu_{\mathrm{TS}}^{\mathrm{ex}} = \mu_{\mathrm{TS}}^{\Gamma} + \rho\left(\mu_1^{\Theta} + \mu_1^{\mathrm{elec}}\right) + (1-\rho)\left(\mu_2^{\Theta} + \mu_2^{\mathrm{elec}}\right), \tag{14}$$

where the parameter ρ is called the asymmetry factor; it is approximately constant between zero and one for numerous reactions [27, 28, 30]. $\mu_{\mathrm{TS}}^{\Gamma}$ is the non-ideal component of the electrochemical potential in the transition state.

In electrochemical equilibrium ($\mu_1 = \mu_2$), the equilibrium electric potential difference, ΔE_{eq}, is expressed as

$$\Delta E_{\mathrm{eq}} = \frac{\mu_2^{\mathrm{diff}} + \mu_0^{\mathrm{M}^{n+}} - \mu_1^{\mathrm{diff}} - \mu_1^{\Gamma}}{nF}\,. \tag{15}$$

When not in equilibrium, corrosion occurs under the activation overpotential, η, defined as

$$\eta = \Delta E - \Delta E_{\mathrm{eq}}\,, \tag{16}$$

Substituting Eq. (15) into Eq. (16), the activation overpotential, η, can be expressed as

$$\eta = \Delta E + \frac{\mu_1^{\Gamma}}{nF} + \frac{\mu_1^{\text{diff}} - \mu_2^{\text{diff}}}{nF} - \frac{\mu_0^{\text{M}^{\text{n+}}}}{nF}. \tag{17}$$

It is observed that the activation overpotential, η, also depends on the elastic strain energy; here, $\mu_1^{\Gamma} = \mu_1^{\text{ex}} = \left(\partial p\left(\bar{c}^{\text{M}}\right)/\partial \bar{c}^{\text{M}}\right) f_{\text{mech}}^{\text{M}}/c_{\text{ref}}^{\text{M}}$. This implies that the sample under stress corrodes more straightforwardly than the sample without stress. Figure 2 illustrates the reaction kinetics that is likely to result from the above formula. Referring to Fig. 1, we consider the scenario in which corrosion occurs under an activation overpotential, η. If the sample is mechanically loaded, the electrochemical potential at the initial state is elevated. Therefore, the electric potential difference (the red arrow in Fig. 2) is smaller than that in the stress-free case (the blue arrow).

Fig. 2

Substituting Eqs. (10)–(14) into Eq. (9c), the reaction rate can be expressed as

$$r_{\text{net}} = k_0 \exp\left(-\frac{\mu_{\text{TS}}^{\Gamma}}{RT}\right)\left(\begin{array}{l} \exp\left(\dfrac{\mu_1^{\text{diff}} + \mu_1^{\Gamma} + (1-\rho)nF\Delta E - (1-\rho)\mu_0^{\text{M}^{\text{n+}}}}{RT}\right) - \\ \bar{c}^{\text{M}^{\text{n+}}} \exp\left(\dfrac{-\rho nF\Delta E + \rho\mu_0^{\text{M}^{\text{n+}}}}{RT}\right) \end{array}\right). \tag{18}$$

By introducing Eq. (17), Eq. (19) can be re-expressed in the form of a generalized Butler–Volmer equation:

$$r_{\text{net}} = k_0 \exp\left(\frac{\mu_{\text{TS}}^{\Gamma} - \rho\left(\mu_1^{\text{diff}} + \mu_1^{\Gamma}\right) - (1-\rho)\mu_2^{\text{diff}}}{RT}\right)\left(\exp\left(\frac{(1-\rho)nF\eta}{RT}\right) - \exp\left(-\frac{\alpha nF\eta}{RT}\right)\right) . \tag{19}$$

Following Chen *et al.* [29], we also assume that the contribution of the elemental concentration gradient, μ_1^{diff} , is significantly smaller than the mechanical and electrical contributions. Thus, we adopt the approximation $r_{\text{net}} \approx r_{\text{net}}\big|_{\mu_1^{\text{diff}}=0} +$

$\left[\left(\partial r_{\mathrm{net}}/\partial\mu_1^{\mathrm{diff}}\right)\Big|_{\mu_1^{\mathrm{diff}}=0}\right]\mu_1^{\mathrm{diff}}$ to express the reaction rate as

$$
\begin{aligned}
r_{\mathrm{net}} = {} & L_S\left(W\frac{\partial g\left(\bar{c}^{\mathrm{M}}\right)}{\partial\bar{c}^{\mathrm{M}}}-\lambda\nabla^2\bar{c}^{\mathrm{M}}\right)+ \\
& L_\kappa\left(\exp\left(\frac{\mu_1^{\Gamma}+(1-\rho)nF\Delta E-(1-\rho)\mu_0^{\mathrm{M}^{\mathrm{n+}}}}{RT}\right)-\bar{c}^{\mathrm{M}^{\mathrm{n+}}}\exp\left(\frac{-\rho nF\Delta E+\rho\mu_0^{\mathrm{M}^{\mathrm{n+}}}}{RT}\right)\right),
\end{aligned}
\tag{20a}
$$

where L_S and L_κ are coefficients expressed as

$$
L_S=\frac{k_0}{RTc_{\mathrm{ref}}^{\mathrm{M}}}\exp\left(-\frac{\mu_{\mathrm{TS}}^{\Gamma}}{RT}\right)\exp\left(\frac{\mu_1^{\Gamma}+(1-\rho)nF\Delta E-(1-\rho)\mu_0^{\mathrm{M}^{\mathrm{n+}}}}{RT}\right)
\tag{20b}
$$

and

$$
L_\kappa=k_0\exp\left(-\frac{\mu_{\mathrm{TS}}^{\Gamma}}{RT}\right).
\tag{20c}
$$

2.3. Governing equation for the mechanico-electrochemical PF model

In the PF model, the phase order parameter, ϕ, can be either an arbitrarily defined order parameter or a physical quantity that differentiates different phases. Herein, the dimensionless concentration of metal (M), being unity in metal and zero in the corrosion product, serves the purpose of differentiating phases. Thus, we set $\phi=\bar{c}^{\mathrm{M}}$. It is apparent that the decrease in the metal phase is owing only to corrosion. Thus, the relation between the reaction rate and phase transformation rate is expressed as $\partial\phi/\partial t = -r_{\mathrm{net}}$. It is observed that the right-hand side of Eq. (20a) is divided into two parts: the interfacial energy (the first term) and the reaction kinetics (the second term). The interfacial energy is spatially continuous, whereas the reaction kinetics is spatially discontinuous, which is not implementable in a numerical scheme. Because corrosion occurs only at the interface ($0 < \phi < 1$), we follow the general treatment in the PF method [27] to use the function $\partial p(\phi)/\partial\phi$ to mollify the discontinuity. Consequently, the rate of phase transformation is expressed as

$$\begin{aligned}\frac{\partial\phi}{\partial t} &= -L_S\left(W\frac{\partial g(\phi)}{\partial\phi}-\lambda\nabla^2\phi\right)- \\ &\frac{\partial p(\phi)}{\partial\phi}L_\kappa\left(\exp\left(\frac{\mu_1^\Gamma+(1-\rho)nF\Delta E-(1-\rho)\mu_0^{\mathrm{M^{n+}}}}{RT}\right)-\overline{c}^{\mathrm{M^{n+}}}\exp\left(\frac{-\rho nF\Delta E+\rho\mu_0^{\mathrm{M^{n+}}}}{RT}\right)\right).\end{aligned} \tag{21}$$

It is noted that Eq. (21) is consistent with a generalized Allen–Cahn type equation, which is convenient for capturing the influences of corrosion, mechanical deformation, and electrostatic potential.

The variation in the concentration of metal cations ($\mathrm{M^{n+}}$) in an electrolyte is governed by the Nernst–Planck equation:

$$\frac{\partial c^{\mathrm{M^{n+}}}}{\partial t}=\nabla\left(D\nabla c^{\mathrm{M^{n+}}}+\frac{DnFc^{\mathrm{M^{n+}}}}{RT}\nabla\varphi\right)-c_{\mathrm{ref}}^{\mathrm{M}}\frac{\partial\phi}{\partial t}. \tag{22}$$

In Eq. (22), the first term on the right-hand side describes the elemental diffusion impelled by the concentration and electric potential gradients. Here, D is the diffusion coefficient of metal cations ($\mathrm{M^{n+}}$), expressed as $D = (D_\mathrm{S})^{p(\phi)}(D_\mathrm{L})^{1-p(\phi)}$; D_S and D_L are the diffusion coefficients of metal cations ($\mathrm{M^{n+}}$) in the solid and liquid phases, respectively. The second term on the right-hand side represents the elemental production (per unit time and unit volume). It is apparent that the elemental production is related to the consumption of metal (M), *i.e.*, the corrosion of a mole of metal (M) releases a mole of metal cations ($\mathrm{M^{n+}}$).

The electrostatic field, φ, is governed by Poisson's equation. We introduce a source term to represent the net change in charge density as a result of electrochemical reaction; this yields

---

$$\nabla\left(-\varepsilon\nabla\varphi\right)=\varsigma \tag{23a}$$

$$\text{and}\quad \varsigma=nFc_{\text{ref}}^{\text{M}}\left(\partial\phi/\partial t\right), \tag{23b}$$

where ε is the electric conductivity of the medium ($\varepsilon = (\varepsilon_{\text{S}})^{p(\phi)}(\varepsilon_{\text{L}})^{1\text{ - }p(\phi)}$). ε_{S} and ε_{L} are the electric conductivities of the solid and liquid phases, respectively. The right-hand side of Eq. (23a), $\varsigma=nFc_{\text{ref}}^{\text{M}}\left(\partial\phi/\partial t\right)$, is the charge–density change per unit time (C m^{-3} s^{-1}) owing to the flow of electrons (e^{-}) in the metal. Note that we omit the change in charge–density owing to ion diffusion by assuming the electric neutrality of the electrolyte.

The stress tensor $\boldsymbol{\sigma} = \mathbf{D}^{\text{e}}\boldsymbol{\varepsilon}^{\text{e}}$ satisfies the equilibrium equation:

$$\text{div}\left(\boldsymbol{\sigma}\right)=0, \tag{24}$$

where div is the divergence operator and the body force is omitted. Substituting Eqs. (5)–(7) into Eq. (24) yields the governing equation of the displacement field $\mathbf{d}$:

$$\text{div}\left[\left(p\left(\phi\right)\mathbf{D}^{\text{e}}\right)\left\{\frac{1}{2}\left(\frac{\partial d_i}{\partial x_j}+\frac{\partial d_j}{\partial x_i}\right)\right\}\right]=0. \tag{25}$$

By defining the reference length, l_{ref}, reference time, t_{ref}, reference energy density, f_{ref}, and reference electric potential, φ_{ref}, the non-dimensional evolution equations can be derived for numerical simulation. (See Appendix A.)

2.4. 1D analytical solution for the rate of charge–density change

Before describing the numerical implementation of the above governing equations, let us discuss the analytical solution; it provides a preliminary understanding of the corrosion behavior and can also be used to validate the numerical scheme. The analytical solution of Eq. (21) can be obtained for the 1D case and under the steady state conditions, *i.e.*, the elemental concentration, electric potential, and elastic energy no longer change with time. The solution is of a hyperbolic-tangent type [33], ϕ =

0.5tanh(3(x - vt) / ζ) + 0.5; here, v is the magnitude of the velocity of the phase boundary migration, along the positive direction of the x axis:

$$v = L_\kappa \zeta \left(\begin{array}{l} \exp\left(\dfrac{f_{\mathrm{mech}}^{\mathrm{M}}\left(\boldsymbol{\varepsilon}^{\mathrm{e}}\right)/c_{\mathrm{ref}}^{\mathrm{M}} + (1-\rho) nF\Delta E - (1-\rho)\mu_0^{\mathrm{M}^{\mathrm{n+}}}}{RT} \right) - \\ \bar{c}^{\mathrm{M}^{\mathrm{n+}}} \exp\left(\dfrac{-\rho nF\Delta E + \rho \mu_0^{\mathrm{M}^{\mathrm{n+}}}}{RT} \right) \end{array} \right). \tag{26}$$

The corresponding phase transformation rate can be obtained as

$$\frac{\partial \phi}{\partial t} = -\frac{6v\phi(1-\phi)}{\zeta}. \tag{27}$$

The negative sign in Eq. (27) represents the consumption of the solid phase during corrosion. Substituting Eqs. (26) and (27) into Eq. (23b), the charge–density change per unit time, ς, can be derived as

$$\varsigma = -6\phi(1-\phi) nFc_{\mathrm{ref}}^{\mathrm{M}} L_\kappa \left(\begin{array}{l} \exp\left(\dfrac{f_{\mathrm{mech}}^{\mathrm{M}}\left(\boldsymbol{\varepsilon}^{\mathrm{e}}\right)/c_{\mathrm{ref}}^{\mathrm{M}} + (1-\rho) nF\Delta E - (1-\rho)\mu_0^{\mathrm{M}^{\mathrm{n+}}}}{RT} \right) - \\ \bar{c}^{\mathrm{M}^{\mathrm{n+}}} \exp\left(\dfrac{-\rho nF\Delta E + \rho \mu_0^{\mathrm{M}^{\mathrm{n+}}}}{RT} \right) \end{array} \right). \tag{28}$$

3. Numerical analysis for mechanico-electrochemical pitting corrosion

Fig. 3

The numerical simulation is intended to study a metal–liquid binary system, as shown in Fig. 3; here, l = 150 μm and h = 300 μm. The metal is covered with a passive film, which exhibits local breakdown, initiating a semi-ellipsoid corrosion pit. The semi-major and semi-minor axes of the semi-ellipse breakdown are set to be a = 20 μm and b = 0–40 μm. Owing to symmetry, only half of the binary system is modeled, as shown in Fig. 3. The initial thicknesses of the metal, liquid phases, and passive film are set as 150 μm, 145 μm, and 5 μm, respectively. The initial phase order parameter, ϕ, and dimensionless metal cation concentration, $\bar{c}^{\mathrm{M}^{\mathrm{n+}}}$, are set as ϕ =

1 and $\bar{c}^{\mathrm{M}^{n+}} = 0$ in the metal phase, and ϕ = 0 and $\bar{c}^{\mathrm{M}^{n+}} = 0$ in the liquid phase.

For the boundary conditions, zero-flux conditions for the phase order parameter, ϕ, are applied to all the sides; moreover, zero-flux conditions for ion concentration are applied to the right, left, and bottom sides. The condition for the outlet boundary [34], wherein the ions should be transported out of the model domain under an electric field, is applied to the upper side to prevent unrealistic ion accumulation at the top. The electrical potentials are φ_{S} and φ_{L} at the bottom of the metal and top of the electrolyte, respectively. The metal is under uniaxial compression with displacement of the left boundary, u_x = 0–3 μm. The top of the metal is unconstrained, and the bottom and right (symmetric axis) are constrained along their normal direction. The intact passive film is assumed to be a zero-flux interface for the phase order parameter, ϕ, ion concentration, $\bar{c}^{\mathrm{M}^{n+}}$, and electrical potential, φ, as indicated in Fig. 3.

The parameters used in the simulation are listed in Table 1; it refers to the scenario in which an iron component is corroded in seawater. COMSOL Multiphysics® modeling software [34] is employed to solve the governing equations based on the FEM. To guarantee the convergence of the solution, the simulation box is discretized by uniform square mesh at a size of 2 μm, *i.e.*, l_{ref} / 5, and the initial and maximum time-steps are both t_{ref} / 100 for the temporal integration. Note that the reference values listed in Table 1, such as t_{ref}, l_{ref}, f_{ref}, φ_{ref}, $c_{\mathrm{ref}}^{\mathrm{M}^{n+}}$, and $c_{\mathrm{ref}}^{\mathrm{M}}$, are only for the conversion from the unitless numerical simulations to the physical scenarios, and can be arbitrarily specified. The reference concentrations of metal and metallic cations, $c_{\mathrm{ref}}^{\mathrm{M}}$ and $c_{\mathrm{ref}}^{\mathrm{M}^{n+}}$, are validated in Appendix A.

Table 1 Parameters used in simulation

	Parameter	Value

Interfacial energy density	S	1 J m^{-2} [19]
Interface thickness	ζ	10 μm [29]
Young's modulus for metal phase	E	150 GPa
Poisson's ratio for oxide phase	v	0.33
Coefficients to scale the contributions of the interfacial energy	L_S	10^{-6} m^3 J^{-1} s^{-1}
Coefficients to scale the contributions of the oxidation kinetics	L_κ	1 s^{-1}
Reference chemical potential of metal cation (M^{n+})	$\mu_0^{M^{n+}}$	RT J mol^{-1}
Asymmetry factor	ρ	0.5
Charge number of metal cation (M^{n+})	n	2
Diffusion coefficients for metal cations in the liquid phase	D_L	5 × 10^{-11}–10^{-8} m^2 s^{-1}
Diffusion coefficients for metal cations in the solid phase	D_S	10^{-14} m^2 s^{-1}
Electric conductivity of liquid	ε_L	1 S m^{-1} [29]
Electric conductivity of metal (M)	ε_S	10^7 S m^{-1} [29]
Reference length	l_{ref}	10 μm
Reference time	t_{ref}	1 s
Reference energy density	f_{ref}	1 GJ m^{-3}
Reference concentration of metal (M)	c_{ref}^{M}	1.403 × 10^2 mol L^{-1} (See Appendix A)
Reference concentration of metal cation (M^{n+})	$c_{ref}^{M^{n+}}$	5.436 mol L^{-1} (See Appendix A)
Reference electrical potential	φ_{ref}	1 mV
Electrical potential at the top side of the liquid electrolyte	φ_L	-300–-1000 mV
Electrical potential at the bottom side of the metal (M)	φ_S	0 mV
Ideal gas constant	R	8.314 J mol^{-1} K^{-1}
Faraday's constant	F	96485 C mol^{-1}

3.1. 1D numerical results for the rate of charge–density change – to verify the code

The numerical scheme was validated based on the 1D analytical solution. In Fig. 3, if the passive layer and the initial corrosion pit are removed, the 2D simulation box is reduced to the 1D problem. To compare with the analytical solution, Poisson's ratio, υ, was set to zero to prevent the Poisson phenomenon. Thus, the elastic energy density in the metal, fM mech, can be conveniently expressed as fM mech = $(1 / 2)E(u_x / l)^2$. Setting $\bar{c}^{\mathrm{M}^{n+}} = 1$ and $\Delta\varphi$ = 0–60 mV, the current I at ϕ = 0.5 can be numerically calculated and compared with the analytical result (Eq. (28)). Figure 4 shows the consistency between the analytical and numerical results; it validates the numerical code. In Fig. 4, $\bar{\varsigma}$ = - ς / ((3 / 2)nFcM refL_κ) is the dimensionless charge–density change per unit time. With the increase in ΔE, the evolution of $\bar{\varsigma}$ exhibits two regimes. When the magnitude of ΔE is low, the linear relation between $\bar{\varsigma}$ and ΔE, known as the Tafel law, can be obtained by an approximation of the analytical solution (Eq. (28)); it is expressed as $\bar{\varsigma} = \left(f^{\mathrm{M}}_{\mathrm{mech}} / c^{\mathrm{M}}_{\mathrm{ref}} + nF\Delta E - \mu_0^{\mathrm{M}^{n+}} \right) / \left(RT \right)$. With further increase in ΔE, $\bar{\varsigma}$ becomes exponentially dependent on ΔE. When $\bar{\varsigma}$ is zero, the equilibrium electric potential difference, ΔE_{eq}, is obtained. It is observed that the equilibrium electric potential difference, ΔE_{eq}, shifts to the left with an increase in u_x. As expressed by Eq. (15), the elastic strain energy may reduce the equilibrium electric potential difference; i.e., a metallic component under mechanical loading (either tension or compression) would be more conveniently corroded than one in a stress-free state.

Fig. 4

3.2. 2D simulation for mechanico-electrochemical pitting corrosion

3.2.1. Pitting corrosion without stress

In this work, the corrosion rate is affected by the diffusion rate as well as the applied electric potential. Therefore, we can explore the transition of pitting corrosion from a diffusion-mediated to an activation-mediated process. Based on the 2D model shown in Fig. 3, we first examine how the corrosion pit evolves from a circular pit with a = 20 μm and b = 20 μm when the metal is stress-free ($u_x = 0$). The effect of the initial geometry on the pitting corrosion is also discussed in the section below.

Figure 5 shows the contour plots of the concentration of metal cations, $\bar{c}^{\mathrm{M}^{n+}}$, and electric potential, φ, at 50 s with an applied electric potential φ_{L} = - 700 mV, and diffusion coefficient $D_{\mathrm{L}} = 5 \times 10^{-11}$–$10^{-9}$ m^2 s^{-1}. It is observed that the pit morphology is semi-circular owing to the approximately uniform distributions of metal cations (Fig. 5(a–c)) and electric potential (Fig. 5(d–f)); this is consistent with previous numerical studies [18-20]. If the diffusion is gradual, the locally released metal cations cannot be completely diluted; this results in a remarkable accumulation of cations near the pit surface and reduces the corrosion rate (Fig. 5(a)). Correspondingly, the larger diffusion rate promotes the corrosion of metal (Fig. 5(b, c)). In Fig. 6, the increase in the corrosion depth, d_{c}, with time, t, for different diffusion coefficients, D_{L}, is plotted. It is observed that the relationship between the corrosion time, t, and corrosion depth, d_{c}, obeys different laws. When the diffusion rate is marginal ($D_{\mathrm{L}} = 5 \times 10^{-11}$ m^2 s^{-1} and 1×10^{-10} m^2 s^{-1} in Fig. 6), the relation between the corrosion time, t, and corrosion depth, d_{c}, is nonlinear after the initial linear relationship. This is because the metal cations cannot be completely diluted at a low diffusion rate. The corrosion rate slows down, and the pitting corrosion transitions from an activation-mediated to a diffusion-mediated process. If the diffusion rate is large (D_{L} =

5×10^{-10} m^2 s^{-1}), the released metal cations can be completely diluted by the liquid electrolyte. Thus, the reaction kinetics rather than the elemental diffusion dominates the pitting corrosion; moreover, the corrosion depth, d_c, exhibits a linear relationship with t.

Fig. 5

Fig. 6

The pitting rate is affected also by the applied electric potential because the latter increases the reaction rate (see Fig. 2), critical cation concentration, $\bar{c}_{\mathrm{cr}}^{\mathrm{M}^{n+}}$ (see Fig. 4(b)), and diffusion rate of metallic cations (see Eq. (28)). To investigate the combined effect of the diffusion rate and applied electric potential, we simulate cases with $D_L = 5 \times 10^{-11}$–10^{-8} m^2 s^{-1}, φ_L = - 300–- 1000 mV, and φ_S = 0 mV.

Fig. 7

Fig. 7(a) shows the variation in corrosion depth d_c at 50 s against D_L and φ_L, where $D_0 = 10^{-8}$ m^2 s^{-1} and φ_0 = -1000 mV are used to normalize D_L and φ_L. It is observed that the relationship between $\log(d_c)$ and φ_L / φ_0 is approximately linear for large D_L. This indicates that the growth of the pits is activation-mediated and obeys the exponential law with φ_L. With the decrease in the diffusion rate, the relationship between $\log(d_c)$ and φ_L / φ_0 becomes more nonlinear on a logarithmic scale. This implies that the pitting corrosion is dominated by the coupling effects of the electrochemical reaction and elemental diffusion. The relationship between $\log(d_c)$ and $\log(D_L / D_0)$ is approximately logarithmic. This implies that the reduction in diffusion rate results in a significant inhibition of pitting corrosion. Because the increases in D_L and φ_L promote the pitting rate, a quantitative analysis is necessary to distinguish the major and secondary influencing factors. The contour of Fig 7(a), in terms of the relation between D_L and φ_L, is plotted in Fig. 7(b). It is observed that the curves relating D_L and φ_L level off at a marginal value of D_L. The curves then gradually inflect and become almost vertical with the decrease in φ_L. Therefore, the line connecting the points of maximum curvature of these contours demarcates the regions where either D_L (Region I) or φ_L (Region II) becomes dominant.

3.2.2. Pitting corrosion under stress

Fig. 8

To exemplify the effect of mechanical deformation, Fig. 8 shows the contour plots of the dimensionless elastic energy density, $\bar{f}_{\text{mech}} = f_{\text{mech}} / f_{\text{ref}}$, at 30 s with $D_L = 10^{-9}$ m^2 s^{-1}, φ_L = - 700 mV, and displacement u_x= 1–3 μm. It is observed that the morphology of the corrosion pit gradually becomes cone-shaped when the deformation u_x increases; this has been observed in previous experimental and numerical studies [35-37]. This is caused by the inhomogeneous distribution of the elastic energy density that is concentrated at the tip of the corrosion pit (see Fig. 8(a–c)). That is, the stress concentration results in a significant increase in local corrosion rate. The evolution of pit morphology and of the dimensionless elastic energy density, $\bar{f}_{\text{mech}} = f_{\text{mech}} / f_{\text{ref}}$, over time for an initially flat metallic surface (a = 20 μm and b = 0 μm) is shown in Fig. 9. It is observed that the nearly flat pit first appears when the material is under an approximately uniform stress (see Fig. 9(a, b)). Then, it develops into a circular pit when the concentrated stress is marginal (see Fig. 9(c)) and finally into a sharpened pit owing to the large stress concentration at the pit tip (see Fig. 9(d–f)).

Fig. 9

Fig. 10

The evolution of the corrosion depth, d_c, with u_x = 0–3 μm is plotted in Fig. 10(a). It is observed that the corrosion depth, d_c, is approximately linearly dependent on t

when $u_x = 0$–2 μm. The variation in the aspect ratio, b / a, of the pit with corrosion time under different displacement boundary conditions is also plotted in Fig. 10(a). It is observed that the aspect ratio increases from one to approximately 1.4 in 30 s when $u_x = 3$ μm; this again demonstrates that the concentrated elastic energy results in the sharpening of the pit. Figure 10(b) shows the maximum elastic energy per mole, f_{mech} / cM ref, electric potential energy per mole, $nF\Delta\varphi$, and maximum concentration near the pit peak with time; here, $nF\Delta\varphi$ is almost unchanged during corrosion, and the concentration $\bar{c}^{\mathrm{M}^{n+}}$ is significantly smaller than the critical value, $\bar{c}_{\mathrm{cr}}^{\mathrm{M}^{n+}}$. When the displacement is marginal ($u_x = 0$–2 μm), the elastic energy is negligible. Thus, the growth of the pit is activation-mediated, manifesting itself with a constant velocity as expressed in Eq. (28). If the displacement is adequately large ($u_x = 3$ μm), the effect of the elastic energy on the corrosion kinetics is non-negligible, and the corrosion rate tends to speed up. The morphology of the pit becomes increasingly sharp; this in turn results in an increase in the elastic energy density at the peak (see Fig. 10(b)). Because the magnitudes of the displacement and Young's modulus are constant, the influence of the pit morphology on the elastic energy density should be finite. Finally, the increase in the elastic energy over time slows down (see Fig. 10(b)), and the corrosion rate approaches a constant value (see Fig. 10(a)).

As mentioned, we study only the compression scenario because it does not cause the propagation of Mode-I cracks. To discuss the crack propagation in a corrosive environment, we refer to a tension scenario. Figure 11(a–d) shows the evolution of the pit and the equivalent stress field, σ_{eq}, when the metallic component has an initially flat breach ($a = 20$ μm and b = 0 μm) under the displacement boundary condition $u_x = -3$ μm.

Fig. 11

It is observed that the maximum equivalent stress increases from an initial 320 MPa to 650 MPa, which may be higher than the yield strength of certain high-strength steels. The tension in the metallic sample may result in the initiation and propagation of Mode-I cracks. Thus, the stress intensity factor, K_{I}, is also calculated based on the strain energy release rate:

$$K_{\mathrm{I}} = \sqrt{-\frac{E}{t_{\mathrm{s}}}\partial\left(\int_{\Omega} f_{\mathrm{mech}} d\omega\right)\Big/\partial d_{\mathrm{c}}}\ . \tag{29}$$

where K_{I} is the stress intensity factor for type I cracks, $\int_{\Omega} f_{\mathrm{mech}} d\omega$ is the total elastic energy in the metallic sample, $t_{\mathrm{s}} = l_{\mathrm{ref}}$ is the thickness of the sample, and $-\partial\left(\int_{\Omega} f_{\mathrm{mech}} d\omega\right)\Big/ t_{\mathrm{s}}\partial d_{\mathrm{c}}$ is the strain energy release rate with the increase in the corrosion depth, d_{c}. Figure 11(e) plots the variation in the stress intensity factor with the depth of the pit. It is observed that the maximum K_{I} is 65.7 MPa $\mathrm{m}^{1/2}$; this exceeds the critical stress intensity factor, K_{IC}, of some high-strength steels (K_{IC} of high-strength steel is in the range of 50–150 MPa $\mathrm{m}^{1/2}$ [38]) and may result in cracking initiation and progression.

Fig. 12

In a complex service environment, pitting corrosion is generally affected by variations in both the applied electric potential and mechanical loading. To elaborate these effects further, numerical studies are carried out. The corrosion lifetime, t_{c}, defines the time required for the corrosion pit to penetrate through the whole metallic sample. The variation in the corrosion lifetime, t_{c}, with the variations in the applied electric potential, $\varphi_{\mathrm{L}} = -300$–$-1000$ mV, and the applied displacement, $u_x = 0$–3 μm is plotted in Fig. 12(a). When the elastic strain energy (in terms of u_x^2 in Fig. 12(a)) and applied electric potential are both marginal, the decrease in the corrosion lifetime is approximately linear with either of the factors (u_x^2 and φ_L). When these two factors are further increased, the decrease in t_c becomes nonlinear; this is consistent with the presumption of Eq. (26) that the corrosion rate is an exponential function of the elastic energy and applied electric potential.

The corrosion lifetime, t_c, is also affected by the applied load and initial geometry of the pit, as shown in Fig. 12(b). For large u_x, the corrosion lifetime is nonlinearly dependent on the initial geometric features (in terms of b in Fig. 12(b)). It is observed that with the increase in b, t_c first decreases rapidly and then approaches a stable magnitude. The corresponding average tip advancement speed, v_c^{tip}, is shown in Fig. 12(c). It is observed that if the material is stress-free, v_c^{tip} is independent of b. When a large displacement (mechanical deformation) is applied to the material, the increase in b results in an elevation in the elastic energy density near the tip; this accelerates pitting and increases the tip advancement speed. Because the influence of the pit morphology on the elastic energy density is finite (as mentioned in the above section), the variation in the elastic energy density near the tip tends toward convergence (see Fig. 12 (d)). Therefore, when b is large, the tip advancement speed approaches a maximum value (see Fig. 12(c)), and the rate of decrease in the corrosion lifetime is reduced (see Fig. 12 (b)).

3.2.3. Pitting corrosion in fiber/particle-reinforced MMCs

Compared with pure metals, fiber/particle-reinforced MMCs exhibit more desirable modulus, strength, thermal stability, and corrosion resistance; they have been widely used in aerospace, automotive, and numerous other applications. Therefore, to extend our simplified model to the scenario of a complicated stress field, an MMC could serve as an effective example. It is observed that the Young's modulus of reinforcement, such as for SiC, varies over a range that could be either higher or lower than that of steel [39]. Therefore, the effect of the relative stiffness on the corrosion behavior is studied here. In a numerical study, only the metal matrix can be corroded. The reinforcing phase is considered to be a ceramic such as SiC, Al_2O_3, or BN, which is uniformly distributed within the matrix. The surfaces of the fiber/particles are thus considered as zero-flux boundaries. The volume fraction of the ceramic fiber/particles was set at 12 vol%, whereas the radius of the fiber/particles varied from 5 to 10 μm. The Poisson's ratio, ν_c, and the Young's modulus, E_c, of the reinforcing phases are 0.33 and $0.5E$–$3E$, respectively. In a simulation, the initial passive film breakdown is flat; therefore, a and b are set to 20 μm and 0 μm, respectively. Figure 12 shows the contour plots of the concentration $\bar{c}^{M^{n+}}$ at 50 s with the fiber/particle radius r = 0–10 μm, diffusion coefficient $D_L = 10^{-9}$ m^2 s^{-1}, applied electric potential φ_L = - 700 mV, and displacement $u_x = 0$. With the reduction in the fiber/particle size, the diffusion path away from the pit is lengthened. Thus, the smaller sized fiber/particles results in a higher local concentration, $\bar{c}^{M^{n+}}$, as shown in Fig. 13(a–c); this impedes the pitting corrosion.

Fig. 13

When an MMC component is under mechanical loading, the effect of the ceramic reinforcement on the pitting corrosion is complex. Based on the 2D phase field model, let us examine the scenarios in which a fiber-reinforced MMC is transversely deformed either by constant displacement or by a constant load at the boundary. Figure 14(a–c) and (d–f) show the contour plots of the elastic energy density in a pure metal and MMC at 30 s under different conditions, as indicated. When the displacement boundary condition is applied, it is observed that a smaller Young's modulus of the reinforcements results in a lower elastic energy density concentration in the matrix near the pit; this reduces the corrosion rate. Thus, the pit in the MMC with $E_c = 0.5E$ (Fig. 14(b)) is shallower than that in the pure metal (Fig. 14(a)); moreover, the MMC with the stiffer fiber (Fig. 14(c)) has a deeper corrosion pit. Conversely, when the MMC is under a constant load, the stiffer reinforcement withstands a higher load; this results in reduced stresses in the matrix and reduced pitting corrosion, as shown in Fig. 14(d–f). Whereas these findings are obtained based on the scenario wherein the fiber-reinforced MMC is under transverse loading, they are valid for longitudinal loading also. In Appendix B, we illustrate the distribution of the elastic energy density in the longitudinally loaded MMC with a 3D pit. The results indicate a corrosion tendency similar to that revealed by the 2D simulation.

Fig. 14

The above results are further summarized in Fig. 15(a) and (b) to provide a quantitative description of the variations in the fraction, ψ_c, and depth, d_c, of the corroded area against the fiber/particle radius, r, and Young's modulus, E_c, respectively. In a stress-free state, the reinforcement phase improves the corrosion resistance; this is manifested by the reduced area or depth, as shown in Fig. 15(a) and (b), respectively. Note that the fiber diameter or particle size also exerts influence. A smaller size results in a higher corrosion resistance. In the case of a fixed displacement, the corrosion resistance of MMC benefits from the decrease in the reinforcement stiffness; meanwhile, if a constant load is applied, the increase in the reinforcement stiffness enhances the corrosion resistance of MMC. In addition, it is observed that the area fraction, ψ_c, increases with the size of the reinforcement. For the pit depth, the larger radius of the reinforcement plays the reverse role; it reduces d_c. Our modeling results provide a guideline for the selection of ceramics fibers/particles for enhancing the corrosion resistance of MMC.

Fig. 15

4. Conclusions

A new PF model to investigate mechanico-electrochemical corrosion is proposed. The mechanico-electrochemical corrosion rate is derived based on a detailed balance of the electrochemical reaction and conforms to a generalized Butler–Volmer equation. The contributions of the chemical potential, metal–electrolyte interface, electrostatic field, and mechanical deformation are included in the Gibbs free energy of the system. Thus, the complete PF model is established by an Allen–Cahn type equation for governing the phase transformation from metallic solid to metal ions in liquid electrolyte, in association with Nernst–Planck equations for diffusion, Poisson's equation for electrostatic field distribution, and the mechanical equilibrium equation for elastic energy density evaluation. The accuracy of the PF model was validated by comparing with the 1D analytical solutions. The equilibrium electric potential difference becomes elastic-energy dependent; this reduces the equilibrium electric potential difference and promotes corrosion.

The pitting corrosion of a pure metal is then simulated in 2D. By varying the diffusion coefficient of metal ions in electrolyte, the evolution of the pitting corrosion from diffusion-controlled to activation-controlled is observed. The corrosion rate's dependence on the diffusion and applied potential also exhibits different laws. A map for distinguishing their dominant roles is established. If the sample is under stress, the inhomogeneous distribution of the elastic energy density, which is concentrated at the pit tip, results in a change in the pit morphology from a semi-circular to a conical shape. The sharper morphology in turn results in an increase in the local elastic energy; this speeds up the local corrosion rate at the pit tip.

Pitting corrosion in MMC is also investigated. Without stress, the decrease in the ceramic particle size lengthens the diffusion path and reduces the corrosion rate compared with those of pure metal. If the MMC is under mechanical loading, the behavior of pitting corrosion becomes more complex depending on how the loading is applied at the boundary. In the case of fixed displacement, the softer reinforcement results in higher corrosion resistance in MMC. Conversely, in the case of a constant load, the stiffer reinforcement results in an increase in the corrosion resistance of MMC.

Acknowledgement

This work was supported by the National Natural Science Foundation of China (No. 51672232), Hong Kong Research Grants Council (PolyU 152140/14E, PolyU 152174/17E), Early Career Scheme (ECS) of the Hong Kong Research Grants Council (Grant No. 25200515, Account Code: F-PP27), and Internal Research Funds of Hong Kong Polytechnic University (Grant No. G-YBDH).

Appendix A

The dimensionless governing equation is

$$\begin{aligned}
&\frac{\partial\phi}{\partial\bar{t}} = -\bar{L}_S\left(\bar{W}\frac{\partial g(\phi)}{\partial\phi} - \bar{S}\,\bar{\zeta}\nabla^2\phi\right) - \\
&\frac{\partial p(\phi)}{\partial\phi}\,\bar{L}_\kappa \exp\left(\frac{f_{\mathrm{ref}}\left(\partial p(\phi)/\partial\phi\right)\bar{f}_{\mathrm{mech}}^{\mathrm{M}}\big/c_{\mathrm{ref}}^{\mathrm{M}} + (1-\rho)nF\varphi_{\mathrm{ref}}\Delta\bar{E} - (1-\rho)\mu_0^{\mathrm{M^{n+}}}}{RT}\right) + , \\
&\frac{\partial p(\phi)}{\partial\phi}\,\bar{L}_\kappa\bar{c}^{\mathrm{M^{n+}}} \exp\left(\frac{-\rho nF\varphi_{\mathrm{ref}}\Delta\bar{E} + \rho\mu_0^{\mathrm{M^{n+}}}}{RT}\right)
\end{aligned} \tag{A.1}$$

$$\frac{\partial\bar{c}^{\mathrm{M^{n+}}}}{\partial\bar{t}} = \bar{\nabla}\left(\bar{D}\bar{\nabla}\bar{c}^{\mathrm{M^{n+}}} + n\frac{\bar{D}\varphi_{\mathrm{ref}}}{RT}F\bar{c}^{\mathrm{M^{n+}}}\bar{\nabla}\bar{\varphi}\right) - \frac{c_{\mathrm{ref}}^{\mathrm{M}}}{c_{\mathrm{ref}}^{\mathrm{M^{n+}}}}\frac{\partial\phi}{\partial\bar{t}}, \tag{A.2}$$

$$\bar{\nabla}\left(-\frac{\varepsilon\varphi_{ref}t_{ref}}{L_{ref}^2 F c_{\mathrm{ref}}^{\mathrm{M}}}\bar{\nabla}\bar{\varphi}\right) = n\frac{\partial\phi}{\partial\bar{t}} \tag{A.3}$$

and

$$\mathrm{div}\left[p(\phi)\left(\bar{\mathbf{D}}^{\mathrm{e}}\right)^{p(\phi)}\left\{\frac{1}{2}\left(\frac{\partial \bar{d}_i}{\partial \bar{x}_j}+\frac{\partial \bar{d}_j}{\partial \bar{x}_i}\right)\right\}\right]=0\,, \tag{A.4}$$

respectively; here, the variables and parameters with the over-head bar are defined as $\bar{L}_S = L_S f_{\mathrm{ref}} t_{\mathrm{ref}}$, $\bar{L}_\kappa = L_\kappa t_{\mathrm{ref}}$, $\bar{S} = S / (f_{\mathrm{ref}} l_{\mathrm{ref}})$, $\bar{\zeta} = \zeta / l_{\mathrm{ref}}$, $\bar{W} = W / f_{\mathrm{ref}}$, $\bar{D} = Dt_{\mathrm{ref}} / l2$ ref, and $\bar{\mathbf{D}}^{\mathrm{e}} = \mathbf{D}^{\mathrm{e}}/f_{\mathrm{ref}}$.

The molar mass and density of the metal (Fe) are m_{Fe} = 56 g mol^{-1} and ρ_{Fe} = 7.9 g cm^{-3}, respectively. Thus, the reference molar concentration of the metal (Fe) cM ref = $\rho_{\mathrm{Fe}}/m_{\mathrm{Fe}}$ = 1.403 × 10^2 mol L^{-1}.

In the present work, the reference concentration of the metallic cation is assumed to be the maximum concentration that is soluble in salt water. We assumed the stable ion cation to be Fe^{2+} in salt water. The solubility of FeCl$_2$ is $S_{\mathrm{FeCl_2}}$ = 0.685 g cm^{-3} (20 °C). If we omit the volume change in solution during dissolution, the maximum concentration of FeCl$_2$ should be $S_{\mathrm{FeCl_2}}/m_{\mathrm{FeCl_2}}$ = 5.436 mol L^{-1}; here, $m_{\mathrm{FeCl_2}}$ = 126 g mol^{-1} is the molar mass of FeCl$_2$. Thus, the reference molar concentration of ion cation (Fe^{2+}) is set to $c_{\mathrm{ref}}^{\mathrm{M^{n+}}}$ = 5.436 mol L^{-1}.

Appendix B

The distribution of the elastic energy densities in the MMC component with a 3D pit is numerically calculated; herein, the longitudinal displacement, u_z = 3 μm, and pressure, P = 200 MPa, are applied. The radius of the fiber reinforcements is set to r = 7.5 μm. The Poisson's ratio, ν_{c}, and the Young's modulus, E_{c}, of the reinforcing phases are 0.33 and 0.5E–2E, respectively. The results are shown in Fig. B1(a–f). It is apparent that when the displacement boundary condition is applied, the elastic energy density at the edge of the corrosion pit increases with the increase in E_{c}; this would promote the corrosion. When the MMC is under a constant load, the stiffer reinforcements take more load; this reduces the stress in the matrix and retards corrosion.

Fig. B1

Appendix C

In the present model, we implicitly assume that the cathode reactions are rapid enough that they do not affect the reactions at the anode. Thus, the effect of the cathodic reaction is not considered. However, if the cathode becomes the rate-limiting electrode, the effect of the cathodic reaction must be considered; this can be incorporated into the framework of the present model. For an example, we consider the pitting corrosion of pure metal (Fe) in dilute sulfuric acid solution (H_2SO_4), as schematically shown in Fig. C1.

Fig. C1

In this case, the corresponding cathodic reaction is $2H^+ + 2e^- \rightarrow H_2\uparrow$. Thus, the diffusion of sulfate (SO_4^{2-}) and hydrogen (H^+) ions in the electrolyte should be incorporated in the present model, in which it is governed by the Nernst–Planck equation in the following form:

$$\frac{\partial c^{\mathrm{SO_4^{2-}}\left(\mathrm{or\ H^+}\right)}}{\partial t} = \nabla\left(D^{\mathrm{SO_4^{2-}}\left(\mathrm{or\ H^+}\right)}\nabla c^{\mathrm{SO_4^{2-}}\left(\mathrm{or\ H^+}\right)} + \frac{2D^{\mathrm{SO_4^{2-}}\left(\mathrm{or\ H^+}\right)}Fc^{\mathrm{SO_4^{2-}}\left(\mathrm{or\ H^+}\right)}}{RT}\nabla\varphi\right), \qquad \text{(C.1)}$$

where the superscripts SO_4^{2-} and H^+ represent the sulfate and hydrogen ions, respectively.

Following Mai *et al.* [21], the cathodic surface movement is negligible. The potential applied at the anode and cathode are set to φ_a and φ_c (indicated in Fig. C1). The cathodic reaction consumes hydrogen ions and requires electron influx. Thus, a flux boundary condition can be established on the cathode surface to ensure that the flux of hydrogen ions diffusing to the cathode surface is equal to the rate of consumption; this is expressed as

$$\mathbf{j}^{\mathrm{H}^+} = -\frac{\mathbf{i}}{F} = -\frac{i_0^{\mathrm{cath}}}{F}\exp\left(\frac{\rho F \eta_{\mathrm{sol|cath}}}{RT}\right)\mathbf{n}, \qquad \text{(C.2)}$$

where $\mathbf{j}^{\mathrm{H}^+}$ is the flux of hydrogen ions to the cathode surface; **i** is the current density of the galvanic reaction; and **n** is the direction normal to the cathode surface. i_0^{cath} and $\eta_{\mathrm{sol|cath}}$ are the reference current density and the overpotential between the electrolyte solution and cathode surface, respectively; both these can be measured during the experiment. Based on the above formulae, the cathodic reaction can be incorporated into the present model.

References

[1] Z. Chen, G. Zhang, F. Bobaru. The Influence of Passive Film Damage on Pitting Corrosion, J. Electrochem. Soc., 163 (2015) C19–C24.

[2] G.S. Frankel, T. Li, J.R. Scully. Perspective—Localized Corrosion: Passive Film Breakdown vs Pit Growth Stability, J. Electrochem. Soc., 164 (2017) C180–C181.

[3] W.R. Parrish, J. Newman, Current distribution on a plane electrode below the limiting current, J. Electrochem. Soc., 116 (1969) 169–172.

[4] W.R. Parrish, J. Newman, Current distributions on plane, parallel electrodes in channel flow, J. Electrochem. Soc., 117 (1970) 43–48.

[5] L. Gal-Or, Y. Raz, J. Yahalom, Mathematical characterization of corrosion currents in local electrolytic cells, J. Electrochem. Soc., 120 (1973) 598–603.

[6] E. McCafferty, Calculation of current distribution in circular corrosion cells, Corros. Sci., 16 (1976) 183–190.

[7] S.M. Sharland, P.W. Tasker, A mathematical model of crevice and pitting corrosion- I. The physical model, Corros. Sci., 28 (1988) 603–620.

[8] S.M. Sharland, P.W. Tasker, A Mathematical Model of Crevice and Pitting Corrosion- II. The Mathematical Solution, Corros. Sci., 28 (1988) 621–630.

[9] Y. Xu, H.W. Pickering, The initial potential and current distributions of the crevice corrosion process, J. Electrochem. Soc., 140 (1993) 658–668.

[10] S.P. White, G.J. Weir, N.J. Laycock, Calculating chemical concentrations during the initiation of crevice corrosion, Corros. Sci., 42 (2000) 605–629.

[11] H. Krawiec, V. Vignal, R. Akid, Numerical modelling of the electrochemical behaviour of 316L stainless steel based upon static and dynamic experimental microcapillary-based techniques, Electrochim. Acta, 53 (2008) 5252–5259.

[12] L.C. Abodi, J.A. DeRose, S.Van Damme, A. Demeter, T. Suter, J. Deconinck, Modeling localized aluminum alloy corrosion in chloride solutions under non-equilibrium conditions: steps toward understanding pitting initiation, Electrochim. Acta, 63 (2012) 169–178.

[13] O. Guseva, J.A. DeRose, P. Schmutz, Modelling the early stage time dependence of localised corrosion in aluminium alloys, Electrochim. Acta, 88 (2013) 821–831.

[14] S. Scheiner, C. Hellmich, Stable pitting corrosion of stainless steel as diffusion controlled dissolution process with a sharp moving electrode boundary, Corros. Sci., 49 (2007) 319–346.

[15] J. Xiao, S. Chaudhuri, Predictive modeling of localized corrosion: an application to aluminum alloys, Electrochim. Acta, 56 (2011) 5630–5641.

[16] S. Sarkar, J.E. Warner, W. Aquino, A numerical framework for the modeling of corrosive dissolution, Corros. Sci., 65 (2012) 502–511.

[17] R. Duddu, Numerical modeling of corrosion pit propagation using the combined extended finite element and level set method, Comput. Mech., 54 (2014) 613–627.

[18] Z. Chen, F. Bobaru, Peridynamic modeling of pitting corrosion damage, J Mech. Phys. Solids, 78 (2015) 352–381.

[19] S.G. Kim, W.T. Kim, T. Suzuki, Phase-field model for binary alloys, Phys. Rev. E, 60 (6) (1999) 7186.

[20] W. Mai, S. Soghrati, R.G. Buchheit, A phase field model for simulating the pitting corrosion, Corros. Sci., 110 (2016) 157–166.

[21] W. Mai, S. Soghrati, New phase field model for simulating galvanic and pitting corrosion processes, Electrochim. Acta, 260 (2018) 290–304.

[22] T. Q. Ansari, Z. Xiao, S. Hu, Y. Li, J. Luo, S.Q. Shi, Phase-field model of pitting corrosion kinetics in metallic materials, npj Comput. Mater., 38 (2018).

[23] W. Mai, S. Soghrati, A phase field model for simulating the stress corrosion cracking initiated from pits, Corros. Sci., 125 (2017) 87–98.

[24] T-T. Nguyen, J. Bolivar, Y. Shi, J. Réthoré, A. King, M. Fregonese, J. Adrien, J-Y. Buffiere, M-C. Baietto, A Phase field method for modelling anodic dissolution induced stress corrosion crack propagation, Corros. Sci., 132 (2017) 146–160.

[25] R.K. Zhu, J.L. Luo, Investigation of stress-enhanced surface reactivity on Alloy 800 using scanning electrochemical microscopy, Electrochem. Commun., 12 (2010) 1752–1755.

[26] F.A. Martin, C. Bataillon, J. Cousty, In situ AFM detection of pit onset location on a 304L stainless steel, Corros. Sci., 50 (2008) 84–92.

[27] K. Ammar, B. Appolaire, G. Cailletaud, F. Feyel, S. Forest, Finite element formulation of a phase field model based on the concept of generalized stresses, Comp. Mater. Sci., 45 (2009) 800–805.

[28] S.-L. Wang, R.F. Sekerka, A.A. Wheeler, B.T. Murray, S.R. Coriell, R.J. Braun, G.B. McFadden, Thermodynamically-consistent phase-field models for solidification, Physica D, 69 (1993) 189–200.

[29] L. Chen, H. W. Zhang, L. Y. Liang, Z. Liu, Y. Qi, P. Lu, J. Chen, and L.Q. Chen, Modulation of dendritic patterns during electrodeposition: A nonlinear phase-field model, J. Power Sources, 300 (2015) 376–385.

[30] M. Z. Bazant, Theory of Chemical Kinetics and Charge Transfer based on Nonequilibrium Thermodynamics, Acc. Chem. Res., 46 (2013) 1144–1160

[31] I. Loginova, J. Ågren, G. Amberg, On the formation of Widmanstätten ferrite in binary Fe-C-phase-field approach, Acta Mater., 52 (2004) 4055–4063.

[32] A.M. Kuznetsov, J. Ulstrup, Electron Transfer in Chemistry and Biology: An Introduction to the Theory, Wiley: Chichester, U.K., 1999.

[33] G. Caginalp, Stefan and hele-shaw type models as asymptotic limits of the phase-field equation, Phys. Rev.A, 39 (1989) 5887–96.

[34] COMSOL Multiphysics Users' Guide. Available from: http://www.comsol.com/.

[35] M. Cerit, K. Genel, S. Eksi, Numerical investigation on stress concentration of corrosion pit, Eng. Fail. Anal., 16 (2009) 2467–2472.

[36] X. Feng, X. Lu, Y. Zuo, N. Zhuang, D. Chen, The Effect of Deformation on Metastable Pitting of 304 Stainless Steel Chloride Contaminated Concrete Pore Solution, Corros. Sci., 103 (2015) 223–229.

[37] Y. Li, W. Liu, W. Yan, J. Deng, H. Li, Mechanism of casing failure during hydraulic fracturing: Lessons learned from a tight-oil reservoir in China, Eng. Fail. Anal., 98 (2019) 58–71.

[38] T.L. Anderson, Fracture Mechanics: Fundamentals and Applications 4th Edition, CRC Press, 2017.

[39] S. Suresh, Fundamentals of Metal-Matrix Composites, Butterworth-Heinemann, 1993.

Figure Captions

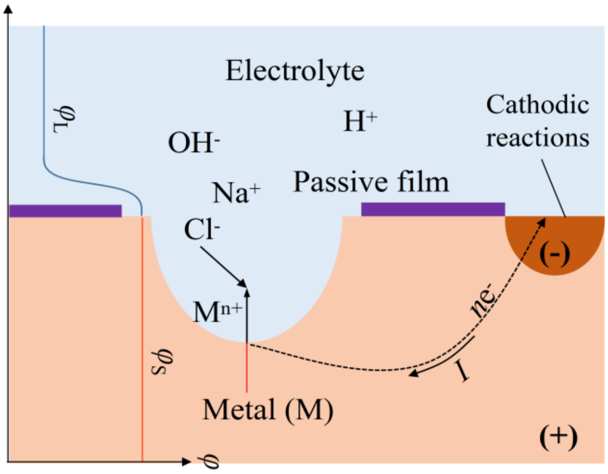

Fig. 1. Schematics of electrochemical corrosion of a pit.

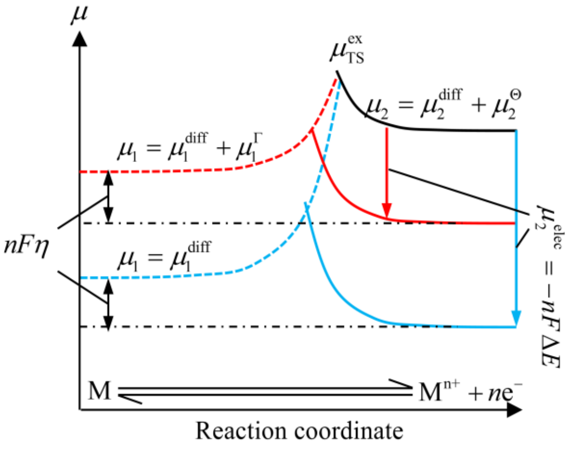

Fig. 2. Landscape of electrochemical potential during reaction.

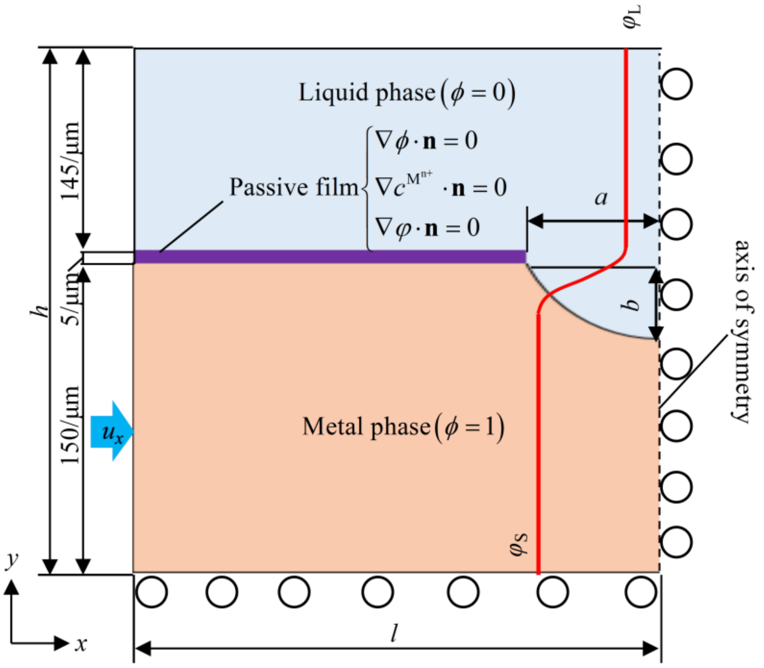

Fig. 3. Geometric and boundary conditions.

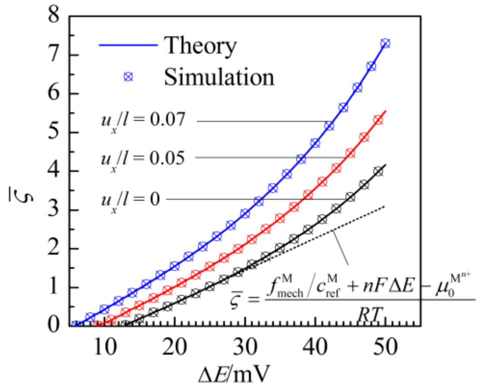

Fig. 4. Variation in dimensionless charge–density change per unit time, $\bar{\varsigma}$, with electric potential difference, Δ*E*, and displacement, u_x.

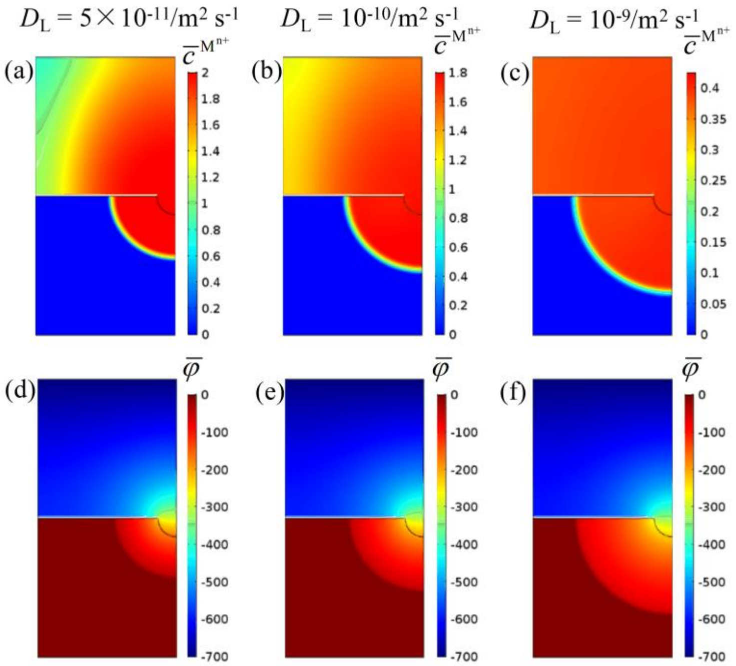

Fig. 5. Contour plots of (a–c) concentration of metal cations, $\bar{c}^{M^{n+}}$, and (d–f) electric potential, φ, at 50 s with applied electric potential φ_L = - 700 mV and diffusion coefficient $D_L = 5 \times 10^{-10}$–10^{-9} m^2 s^{-1}.

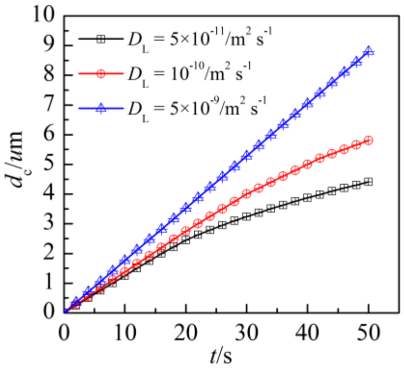

Fig. 6. Evolution of corrosion depth, d_c, with different diffusion coefficient values, D_L.

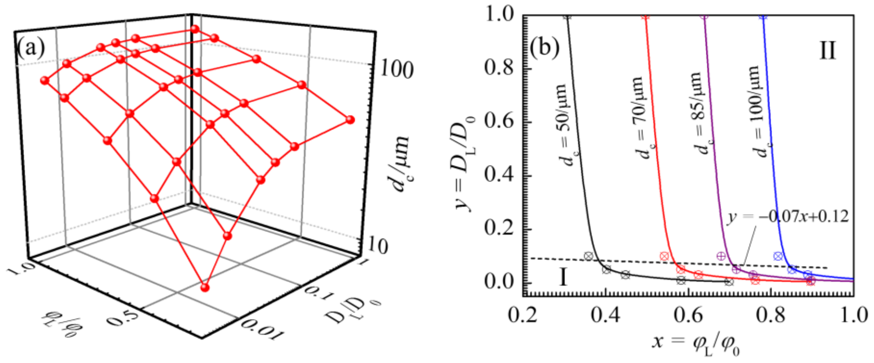

Fig. 7. (a) Variation in corrosion depth, d_c, at 50 s, with respect to the change in D_L and φ_L, and (b) corrosion depth, d_c, diagram with applied electric potential, φ_L, along the x axis and diffusion coefficient, D_L, along the y axis.

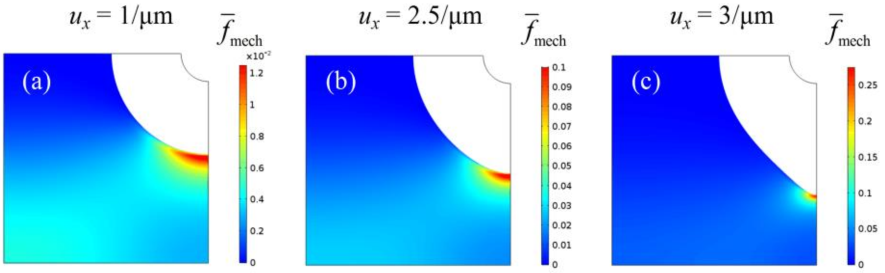

Fig. 8. Contour plots of (a–c) elastic energy density at 30 s with applied electric potential φ_L = - 700 mV and displacement u_x = 1–3 μm.

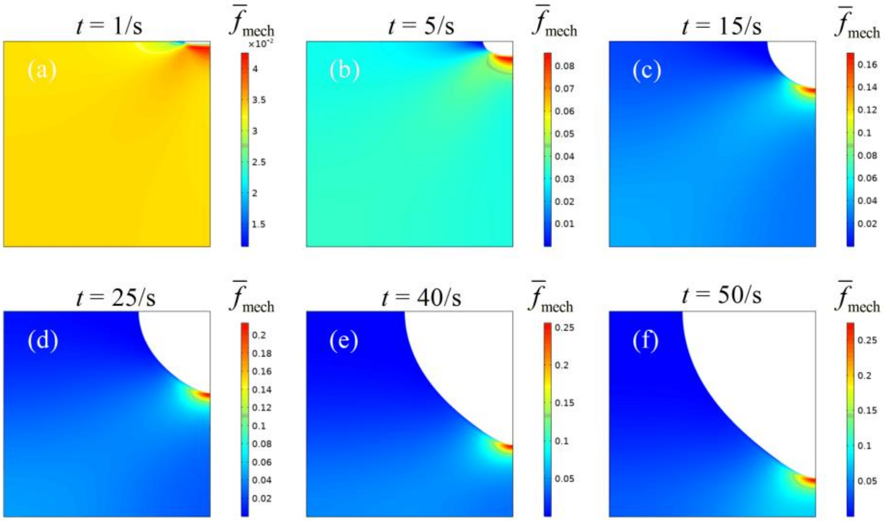

Fig. 9. Evolution of pit morphology and dimensionless elastic energy density, $\bar{f}_{\text{mech}} = f_{\text{mech}} / f_{\text{ref}}$, over time for an initially flat metal surface (a = 20 μm and

$b = 0$ μm) when $u_x = 3$ μm.

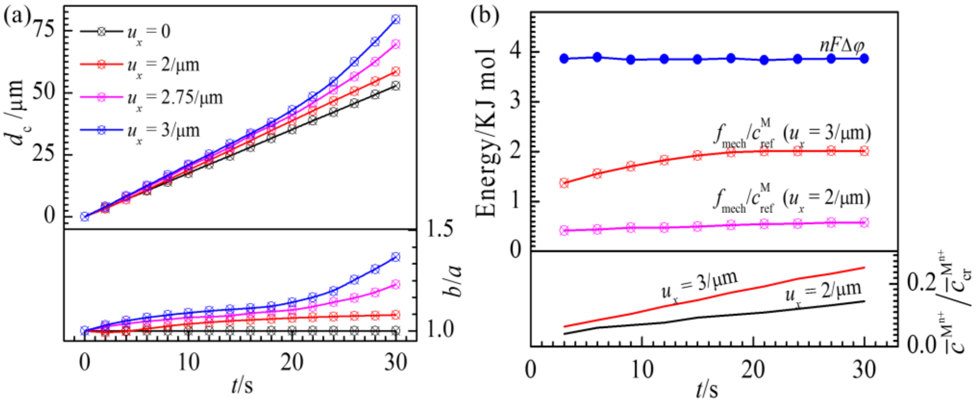

Fig. 10. (a) Evolution of corrosion depth, d_c, and aspect ratio, b / a, of pit with u_x, and (b) evolution of elastic energy, electric potential energy, and concentration.

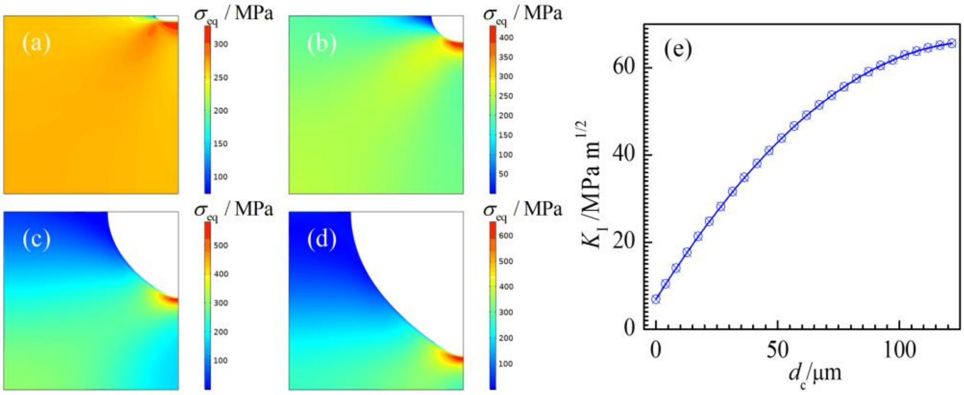

Fig. 11. (a)–(d) Equivalent stress, σ_{eq}, evolution with displacement, $u_x = -3$ μm, in the metallic sample with an initially flat breach ($a = 20$ μm and $b = 0$ μm); (e) evolution of stress intensity factor for type I crack, K_I, with corrosion depth, d_c.

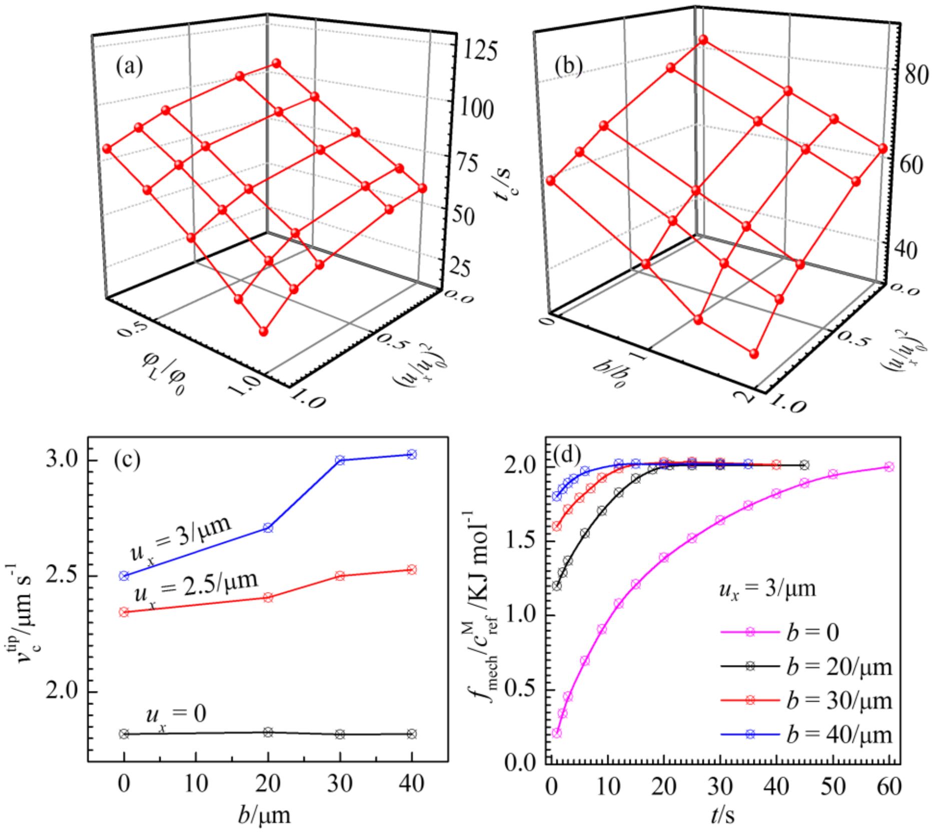

Fig. 12. Evolution of corrosion life, t_c, with (a) the square of displacement, u_x^2, and applied electrical potential, φ_L, (b) the square of displacement, u_x^2, and semi-minor axes of initial pit, b, (c) the average tip velocity of the corrosion pit, v_c^{tip}, in the y direction with u_x = 0–3 µm and b = 0–40 µm, and (d) the evolution of elastic energy for u_x = 3 µm and b = 0–40 µm.

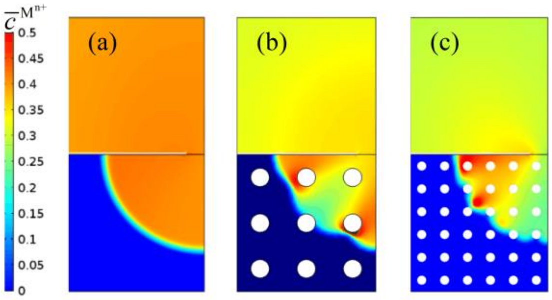

Fig. 13. Contour plots of concentration, $\bar{c}^{M^{n+}}$, at 50 s with particle radius (a) r = 0 (pure metal), (b) r = 10 µm, and (c) r = 5 µm.

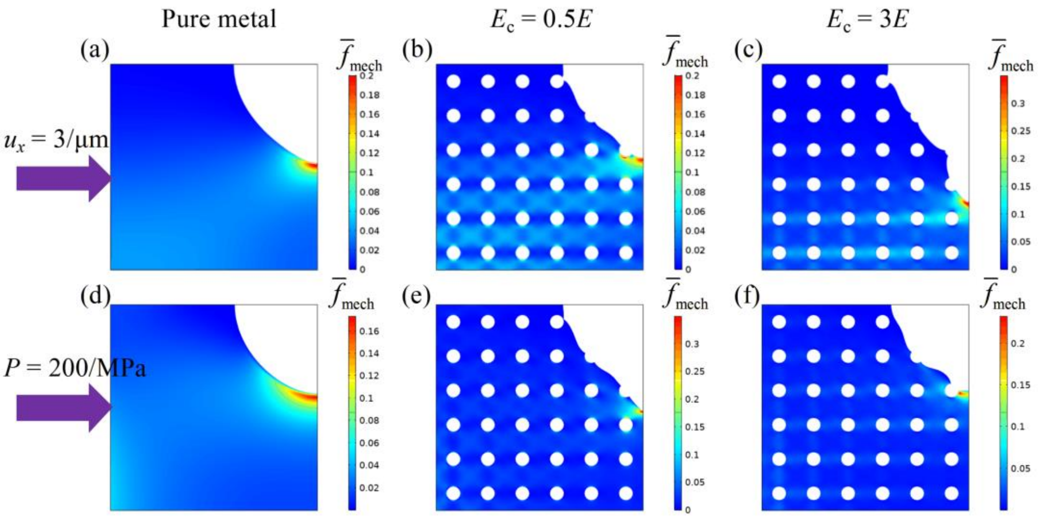

Fig. 14. Contour plot of elastic energy density in pure metal and MMC with $E_c = 0.5E$ and $3E$ at 30 s under the loading of (a–c) displacement, $u_x = 3$ μm, and (d–f) pressure, $P = 200$ MPa.

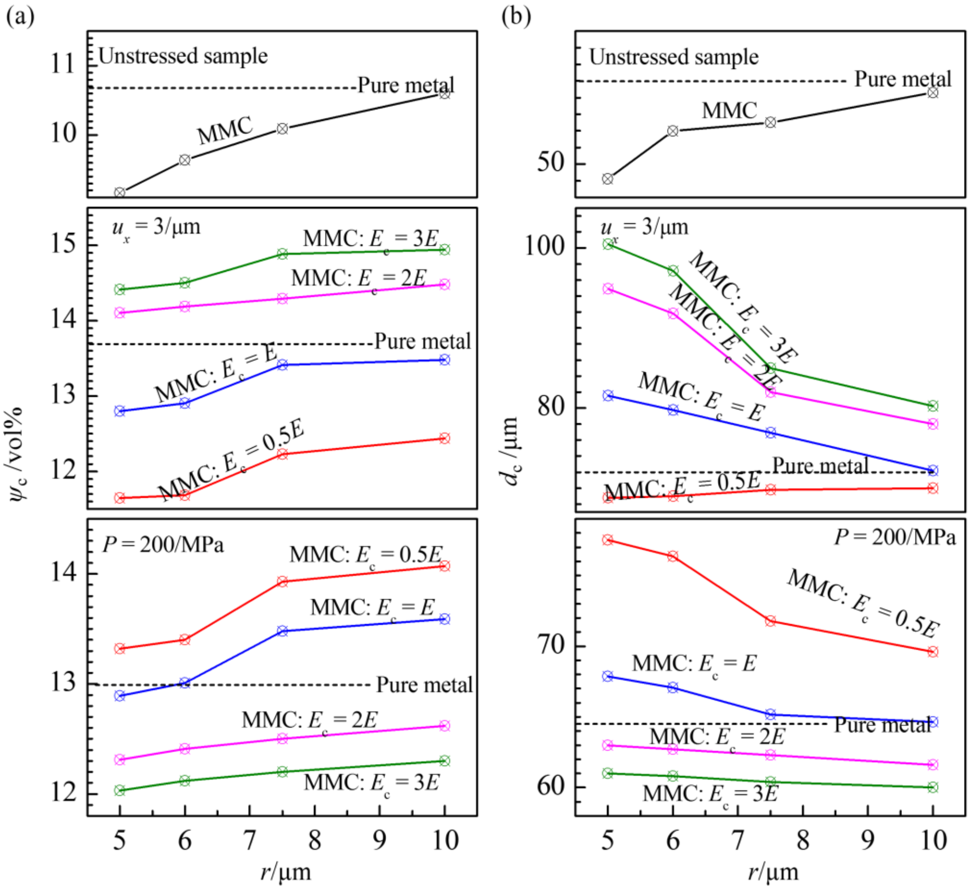

Fig. 15. Evolution of (a) volume fraction of corrosion area, ψ_c, and (b) corrosion depth, d_c, at 30 s with fiber/particle radius, r, and Young's modulus, E_c.

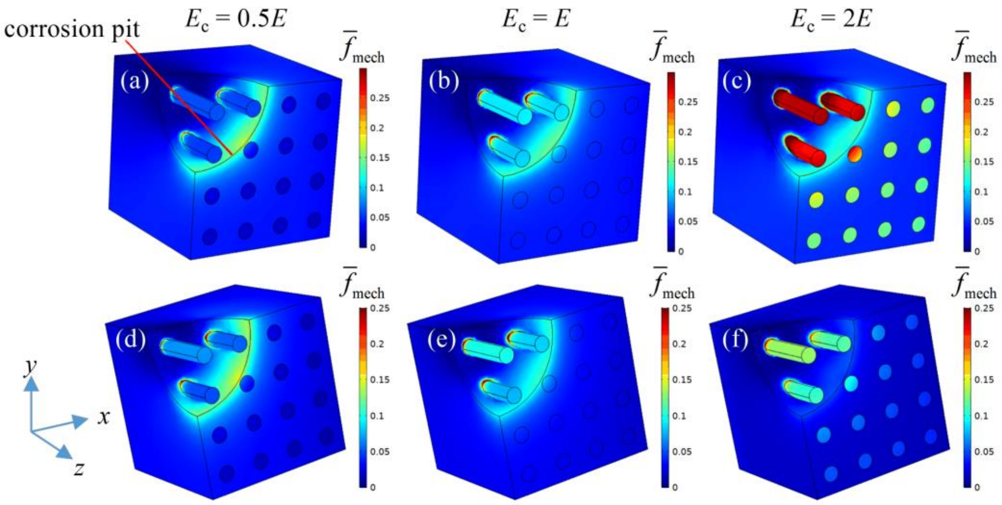

Fig.B1. Contour plot of elastic energy density with (a–c) displacement, $u_z = 3$ μm and (d–f) longitudinal pressure, $P = 200$ MPa.

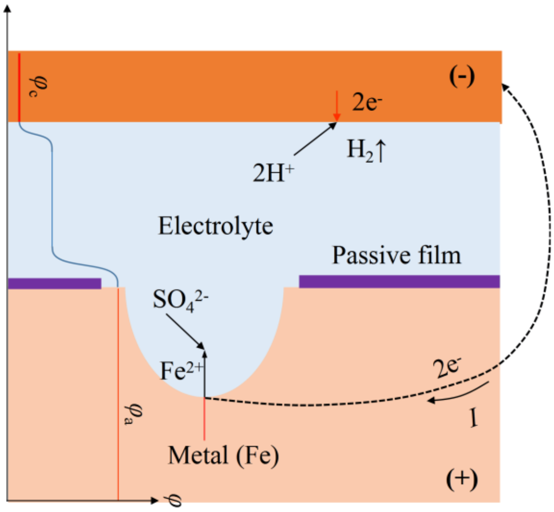

Fig.C1. Schematics of galvanic and pitting corrosion of pure metal (Fe) in dilute sulfuric acid solution.